PAPER

NJC
www.rsc.org/njc

Structure and UV-Vis spectroscopy of the iron-sulfur dinuclear nitrosyl complexes $[Fe_2S_2(NO)_4]^{2-}$ and $[Fe_2(SR)_2(NO)_4]$

Maria Jaworska*[a] and Zofia Stasicka[b]

[a] *Department of Theoretical Chemistry, University of Silesia, Szkolna 9, 40-006 Katowice, Poland. E-mail: mj@ich.us.edu.pl*
[b] *Faculty of Chemistry, Jagiellonian University, Ingardena 3, 30-060 Kraków, Poland. E-mail: stasicka@chemia.uj.edu.pl*

Received (in Montpellier, France) 22nd June 2004, Accepted 15th October 2004
First published as an Advance Article on the web 3rd February 2005

Calculations of the electronic structure, geometry and electronic spectra of Roussin's red salt dianion (RRS) and Roussin's red diester (RRE) were carried out with the RB3LYP and UB3LYP methods. The electronic structure emerging from these calculations may be described as composed of two $\{Fe(NO)_2\}^9$ units, in which ferric ion ($S = 5/2$) is antiferromagnetically coupled to two NO^- ligands (each with $S = 1$), giving $S = 1/2$; the units are antiferromagnetically coupled to each other yielding a total $S = 0$. The S^{2-} bridges (in RRS) or SR^- bridges (RRE) mediate the antiferromagnetic coupling. The character of the frontier orbitals controls the dinuclear species' reactivity, which is initiated by electrophilic attack on S-localized HOMO orbitals (RRS) or nucleophilic attack on the Fe–S antibonding LUMO orbital (RRE). The contrasting susceptibility to electrophilic/nucleophilic attack is also assisted by the sulfur charge, which is negative in RRS and positive in RRE. The calculated spectra of RRS and RRE show substantial resemblance to the experimental spectra. The calculated transitions are mainly of charge transfer character: At long wavelengths they are described as $\pi^*_{NO} \rightarrow$ d (LMCT), at short wavelengths (below 250 nm) the most intense transitions are d $\rightarrow \pi^*_{NO}$ (MLCT). In the middle part of the spectra both types of transitions are present. Some contribution of sulfur to the transitions throughout the whole spectrum is observed. The $\pi^*_{NO} \rightarrow$ d transitions are assumed to be responsible for the photochemical reactivity of both compounds, which is initiated by photodissociation of the NO group.

1. Introduction

Iron-sulfur clusters constitute an integral part of several natural structures occurring in a large family of biologically relevant metalloproteins. These [Fe–S] units form the active sites of enzymes, which play a crucial role in living organism processes such as: electron transfer chain, photosynthesis (photosystem I), isomerization, respiratory chain, nitrogen fixation and many various catalytic reactions; they can also operate as biosensors for oxidants and iron.[1–3] The [Fe–S] clusters are even supposed to be the interface between the biological and inorganic worlds, because they catalyze redox transformations of such likely components of the Earth's primordial atmosphere, as N_2, CO and H_2.[4]

The iron-sulfur units form mono, di-, tri-, tetra- and hexanuclear species in which iron atoms are connected through S bridges, with thiolates as terminal ligands. From the point of view of magnetic properties they can be considered as high-spin ferrous (Fe^{2+}, $S = 2$) or ferric (Fe^{3+}, $S = 5/2$) units antiferromagnetically coupled to each other, where S^{2-} bridges mediate the antiferromagnetic interactions.[5–9]

Quantum mechanical calculations have been widely used to elucidate the electronic structure and interpret the physical properties of such clusters. For iron-sulfur clusters, the iron d-d interactions are weak and the closed-shell wave function is unstable to perturbations that allow electron spins to localize at the iron centres. This led to the idea of spin and space unrestricted wave functions, which provide an improved description of exchange correlation effects. In such wave functions the orbitals describing α (spin-up) and β (spin-down) tend to be localized on different metal atoms. This broken-symmetry (BS) formalism has been used to calculate properties of iron-sulfur clusters such as Heisenberg antiferromagnetic coupling constants and redox potentials.[5–9] The spin unrestricted wave function is not an eigenfunction of the $\langle S^2 \rangle$ operator. The wave function of antiferromagnetically coupled dinuclear complexes has a multiconfigurational character, which is included in the unrestricted DFT wave function.

The interaction of NO with the natural [Fe–S] clusters gives rise to iron-sulfur cluster nitrosyl complexes. These include: $[Fe_2S_2(NO)_4]^{2-}$ (dianion of 'Roussin's red salt', RRS), $[Fe_2(SR)_2(NO)_4]$ (Roussin's red esters, RRE, R = alkyl or aryl), $[Fe_4S_3(NO)_7]^-$ ('Roussin's black salt' anion, RBS) and $[(FeNOS)_4]$ (tetranitrosyltetra-μ_3-sufidotetrahedrotetrairon, 'cubane'). The complexes are reported to act as NO-donor drugs and they are also generated under physiological conditions; some of them, for example, $[Fe_2(SCH_3)_2(NO)_4]$, can be found in natural sources.[10–12]

In this work two dinuclear complexes (RRS and RRE, with R = CH_3) are investigated in order to determine conclusively an explanation of their magnetic, spectral, chemical and photochemical behaviour. The broken-symmetry, spin unrestricted methodology is used in analogy to that applied for iron-sulfur proteins.[5–7] Calculations on the di- and tetranuclear nitrosyl iron-sulfur complexes were done previously with the EHM method.[13]

The class of dinuclear metal complexes with bridging ligands, which are not well-described by the one determinant restricted MO scheme, covers a very wide range of species. Many of them exhibit antiferromagnetic coupling between the metal centres,[14a,14b] as shown by physical measurements. For such systems the broken-symmetry version of the DFT method is usually employed. This applies also to one class of metal–

DOI: 10.1039/b409519g

ligand antiferromagnetically coupled systems, with so-called "non-innocent" ligands.[14c–14e]

2. Method of calculation

The Gaussian03 programme[15] was used in the calculations, which were performed using the DFT method with the B3LYP functional.[16] The electronic spectra were calculated by the TD-DFT method.[17] The basis set used comprised the LANL2DZ basis with the effective core potential of Hay and Wadt[18] on Fe and S with an additional d function on iron ($\alpha = 0.1214$) and on sulfur ($\alpha = 0.7$), DZV (P) basis on N, C and O and DZV on H.[19] To account for the influence of the solvent, the PCM model[20] was used with water as solvent. The non-equilibrium TD-PCM method[21] was employed for the calculations of the electronic spectra in water solution. This method takes into account the solvent relaxation effects, which are important especially in polar environment, to reproduce quantitatively the observed solvent shifts. Calculations were done with the RB3LYP and UB3LYP methods. The unrestricted, broken-symmetry wave functions were obtained by the use of the STABLE (RUHF) option in the Gaussian03 programme.

3. Results and discussion

3.1 $[Fe_2S_2(NO)_4]^{2-}$ (dianion of Roussin's red salt, RRS)

3.1.1 Geometry and electronic structure. The calculations were performed for the singlet spin state, which is the experimental state of RRS. The geometry of RRS optimized at the RB3LYP and UB3LYP levels without any symmetry constraints gives the same result as with the D_{2h} symmetry. The molecule is presented in Fig. 1 and the optimized geometry parameters are collected in Table 1, together with experimental data for RRS.[22] The iron-iron distance in iron-nitrosyl complexes varies from 2.64 Å in cubane, $[Fe_4S_4(NO)_4]$, to 2.72 Å in red diethyl ester and the iron-nitrogen distance varies from 1.63 to 1.67 Å.[23–26] In RRS the experimental distance amounts to 2.716 (2.718) Å and the RB3LYP calculated value is in very good agreement with this value. The UB3LYP bond distances are too long (the Fe–Fe distance is 0.17 Å longer than the experimental one). Because of this the RB3LYP geometry was used for further calculations.

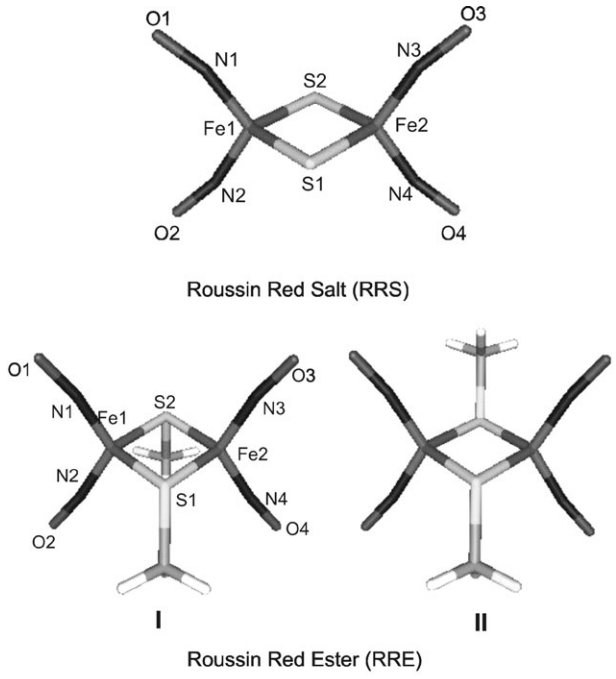

Fig. 1 Roussin's red salt dianion (RRS), $[Fe_2S_2(NO)_4]^{2-}$, and Roussin red methyl ester (RRE), $[Fe_2(SR)_2(NO)_4]$ (conformers I and II).

For the optimized geometry the UB3LYP wave function was determined with the use of the PCM model with water as solvent. As found previously for negatively charged mononuclear nitrosylthiolatoferrate complexes,[27] the 4p iron orbitals contribute significantly to the low energy transitions calculated without any solvent. In the case of negatively charges species the diffuse character of the electron density is responsible for this effect. Because of this, the spectrum of RRS presented in the next section was calculated with the PCM model.

In Fig. 2 several HOMO and LUMO UB3LYP spin-up (α) orbitals of RRS are presented. The UB3LYP spin-up (α) and spin-down (β) orbitals are partially localized on the different parts (left or right) of the molecule. Only α orbitals are presented in Figs. 2, the β orbitals are mirror reflections with regard to the plane crossing the sulfur atoms. The HOMOs are mostly metal-nitrosyl bonding orbitals and the LUMOs are metal-nitrosyl antibonding orbitals of the π type. The H47–H49 orbitals have a high participation of the π^*_{NO} orbitals and they are localized on the left side of the molecule. The H50 (α) orbital is the iron-sulfur bond, which shows the mediation of sulfur in the antiferromagnetic coupling.

The L54 orbital may be viewed as the antibonding σ* metal-metal bond. The LUMO α orbitals of mainly d character are localized on the left side of the molecule (L55, L57, L59 and L61); the orbitals of the π^*_{NO} type are localized on the right side (L56 and L60).

The total energies, atomic charges and spin densities are gathered in Table 2 for the UB3LYP wave function. The iron charge has a small positive value. The negative charge of the $[Fe_2S_2(NO)_4]^{2-}$ anion is spread out almost uniformly onto the sulfur and NO ligands, thus the charges on the NO ligands are in each case negative, with a non-homogeneous charge distribution within the ligand. The UB3LYP calculations show large spin densities on the iron atoms of opposite signs. The NO spin densities are about 1 and have opposing signs to the spin density of the iron atom to which the NO group is bonded. The spin densities from calculations with the solvent model show a similar pattern. The electronic structure of RRS emerging from the UB3LYP broken-symmetry wave function can be described as two $\{Fe(NO)_2\}^9$ units of $S = 1/2$ antiferromagnetically coupled to each other through S^{2-} bridges. In each such unit the ferric ion with $S = 5/2$ is antiferromagnetically coupled to two NO^- ions with $S = 1$. The obtained spin structure of RRS is presented in Scheme 1. This result is similar to that obtained by Noodleman *et al.*[6] for dimer iron-thiolate complexes with sulfur bridges. The iron atoms in such complexes are antiferromagnetically coupled, with an antiparallel spin alignment, each iron atom having a spin quantum number $S = 5/2$. In the RRS case studied here an additional antiferromagnetic spin coupling between the nitrosyl ligands and metal atoms takes place. It may be noted that the spin densities on the iron atoms are much smaller than 5 and on nitrosyls smaller than 2. This is because the localized orbitals are non-orthogonal, which implies that the valence structure in Scheme 1 has a large participation in the total wave function, but other valence structures like Fe^{II}–NO^0 will also contribute.

A qualitative description of the geometry dependence of the metal-NO fragment on the electronic configuration of the $\{M(NO)_x\}^n$ (with $x = 1, 2$) group was given by Enemark and Feltham[28] and others.[29,30] Six-coordinated nitrosyl-iron mononuclear complexes with the $\{Fe(NO)\}^7$ core possess an $S = 3/2$ or 1/2 ground state. It has been shown by X-ray absorption, resonance Raman, MCD, EPR, Mössbauer spectroscopy and DFT calculations that the $\{Fe(NO)\}^7$ ($S = 3/2$) species are high-spin ferric ($S = 5/2$) antiferromagnetically coupled to NO^- ($S = 1$).[31–34] The calculations on mononuclear nitrosylthiolatoferrate complexes, $[Fe(SR)_3(NO)]$ and $[Fe(SR)_2(NO)_2]$, showed that in such complexes the high-spin iron atom

Table 1 RB3LYP (UB3LYP in parentheses) optimized geometry parameters (in Å and °) for RRS, RRE(I) and RRE(II)

	RRS		RRE(I)[a]	RRE(II)	
	Calcd	Exptal[b]	Calcd	Calcd	Exptal[c]
Fe1–Fe2	2.718 (2.884)	2.716, 2.718	2.623 (2.959)	2.623 (2.959)	2.72
Fe1–N	1.618 (1.797)		1.635 (1.736)	1.631 (1.736)	1.67
N–O	1.208 (1.214)		1.175 (1.180)	1.175 (1.180)	1.17
Fe–S	2.266 (2.338)	2.229, 2.249	2.251 (2.406)	2.251 (2.406)	2.27
S–C	—		1.834 (1.843)	1.834 (1.843)	1.84
S1–S2	3.626 (3.684)	3.562, 3.587	3.660 (3.773)	3.660 (3.773)	3.63
Fe1–S1–Fe2	106.3 (103.8)		108.7 (103.4)	108.7 (103.4)	
S1–Fe1–S2	73.7 (76.1)		71.2 (75.9)	71.2 (75.9)	
Fe1–N1–O1	163.2 (157.8)	165.4, 166.2	168.4 (170.6)	169.9 (170.6)	167
N1–Fe1–N2	112.7 (106.2)		118.4 (120.0)	118.4 (120.0)	117

[a] Average values. [b] Ref. 22. [c] Ref. 23.

($S = 5/2$) is also antiferromagnetically coupled to one or two NO^- with $S = 1$.[27]

3.1.2 Electronic spectrum. The electronic spectrum of RRS has three intense bands at 374 ($\varepsilon = 1.04 \times 10^4$), 314 ($0.85 \times 10^4$) and 242 ($2.8 \times 10^4$) nm, and it tails to long wavelengths (above 500 nm).[35–37] Calculations of the electronic spectrum were performed for the UB3LYP and RB3LYP wave functions with the solvent model. Fig. 3 shows the calculated spectrum of RRS obtained from the UB3LYP method with the PCM model. Each calculated transition is drawn as a Gaussian function with the height equal to its oscillator strength and the width equal to 0.09. The experimental spectrum of RRS is also presented in Fig. 3. The spectrum calculated with the RB3LYP method is very similar but shows intense transitions at wavelengths above 500 nm. The transitions with high intensity at long wavelengths are the result of exaggerating the electronic density on the metal-metal axis. There is no band of high intensity in this range in the experimental spectrum. The shape of the spectrum calculated with the UB3LYP method better reproduces the experimental spectrum, and in the following we describe only the transitions found with the UB3LYP method. The calculated electronic transitions with the solvent model in the UB3LYP formalism are summarized in Table 3. Only transitions with fairly large oscillator strengths are listed, except for the longest wavelength transitions, where those with small oscillator strengths were also presented.

There are several transitions at long wavelengths, at about 500, 600 and 700 nm with very small oscillator strengths. They occur from the orbitals of predominantly S_π character to the d orbitals of iron and π* orbitals of nitrosyls. These transitions have small or medium oscillator strengths and they may be responsible for the long wavelength tail in the RRS spectrum.

The two transitions at 418.4 and 391.4 nm are $S_\pi \rightarrow \pi^*_{NO}$, $\pi^*_{NO} \rightarrow$ d, d $\rightarrow \pi^*_{NO}$ in character, with a participation of the sulfur orbitals. There is no discrete band around 400 nm in RRS, but the band may be hidden in the tail of a stronger neighbouring band.

The transition with large oscillator strength ($f = 0.1179$) at 340.6 nm is of $\pi^*_{NO} \rightarrow$ d character and may be ascribed to the band at 374 nm in the experimental spectrum. The transition

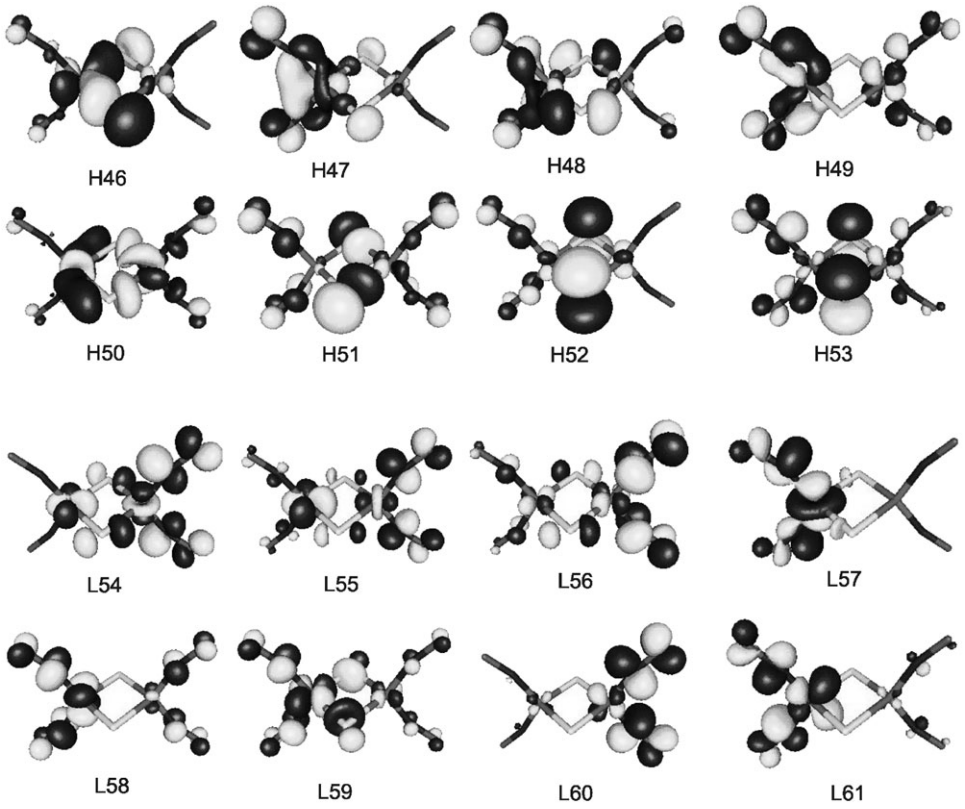

Fig. 2 UB3LYP α (spin-up) HOMO and LUMO orbitals of RRS (PCM solvent model, water as solvent).

Table 2 Total energies, atomic charges and spin densities for RRS and RRE (W = water)

	RRS [UB3LYP(W)]	RRE(I) (UB3LYP)	RRE(II) (UB3LYP)
E/a.u.	−787.329 35	−866.888 267	−866.888 419
$\langle \hat{S}^2 \rangle$	2.795	2.492	2.496

	Charge	Spin	Charge	Spin	Charge	Spin
Fe1	0.074	2.259	0.092	2.146	0.091	2.146
S1	−0.429	0.000	0.161	0.000	0.162	0.000
C1	—	—	0.071	0.000	0.071	0.000
N1	−0.091	−0.476	−0.050	−0.375	−0.050	−0.383
O1	−0.231	−0.398	−0.109	−0.388	−0.112	−0.391
N2	−0.091	−0.496	−0.049	−0.388	−0.050	−0.383
O2	−0.231	−0.398	−0.115	−0.392	−0.112	−0.391
Fe2	0.074	−2.259	0.092	−2.147	0.091	−2.146
S2	−0.429	0.000	0.161	0.000	0.162	0.000
C2	—	—	0.071	0.000	0.071	0.000
N3	−0.091	0.476	−0.050	0.389	−0.050	0.383
O3	−0.231	0.398	−0.109	0.392	−0.112	0.391
N4	−0.091	0.496	−0.049	0.376	−0.050	0.383
O4	−0.231	0.398	−0.115	0.388	−0.112	0.391

with the largest oscillator strength at 307.8 nm ($f = 0.1005$) has d → π^*_{NO} character. It can be assigned to the experimental band at 314 nm.

The transitions at 248.4 and 244.1 nm with very large oscillator strengths can be responsible for the experimental band at 242 nm. The transitions are due predominantly to a d → π^*_{NO} excitation. These transitions have also a large participation of sulfur orbitals.

The calculations in the UB3LYP formalism with the solvent model reproduce the most important features of the experimental spectrum of RRS. Some of the calculated bands are somewhat shifted to shorter wavelengths, but in general the agreement with experiment is good. The transitions are mainly LMCT and MLCT in character, the former prevail at longer wavelengths, the latter are important at the shorter wavelengths. In the entire calculated spectrum the participation of sulfur orbitals in electronic transitions is noticeable.

3.1.3 Chemical reactivity. The $[Fe_2S_2(NO)_4]^{2-}$ anion is stable in alkaline medium; in other conditions (especially in non-aqueous solvents) it aggregates easily to yield polynuclear cluster structures: $[Fe_4S_3(NO)_7]^-$, $[Fe_5S_4(NO)_8]^-$ or $[Fe_7S_6(NO)_{10}]^-$.[10,12,38] The aggregation reactions are accompanied by the formal release from the initial RRS of one S^{2-} and 1, 2 or 4 NO^- ligands for tetra-, penta- and heptanuclear species, respectively. The protonated intermediates, $[Fe_2S(SH)(NO)_4]^-$ and $[Fe_2(SH)_2(NO)_4]$, were identified,[38,39] which suggests that the reaction is initiated by an electrophilic attack and the decreased anion charge of the protonated species facilitates interaction between the dinuclear species. RRS is also well-known to react readily with halogenoalkanes and this reaction has been extensively exploited for the synthesis of the RRE.[40,41]

The electrophilic attack, which initiates the RRS reactivity, takes place on the bridging sulfur atoms. This assumption is consistent with the character of the HOMO orbitals: three of them (H51–H53) are mostly localized on the S atoms (Fig. 2). Association of an electrophile is facilitated by the negative charges of both the S atoms in RRS (Table 2).

The photochemical reactivity of $[Fe_2S_2(NO)_4]^{2-}$, upon 355 nm excitation, leads in the presence of O_2 to $[Fe_4S_3(NO)_7]^-$. Although the product is the same as in the thermal reaction, the mechanism suggested from the flash experiments is quite different.[35,37] The photochemical aggregation is initiated by dissociation of the NO group and further reactivity of the $[Fe_2S_2(NO)_3]^{2-}$ intermediate. This can be interpreted by the UB3LYP calculations, which show that the transitions ascribed to the band at 374 nm in the experimental spectrum are mostly of π^*_{NO} → d (LMCT) character (Table 3). Reactive decay of the excited states should lead readily to Fe–NO bond cleavage.

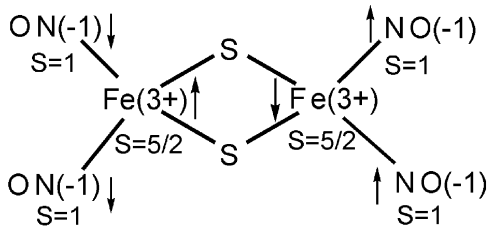

Scheme 1 Spin structure of RRS.

3.2 $[Fe_2(SR)_2(NO)_4]$ (Roussin's red ester, RRE)

The calculations were performed for R = CH_3. The two conformers of RRE existing in solution[42] are depicted in Fig. 1. For the dimethyl derivative the abundance of the two conformers is equal in solution.[12,14]

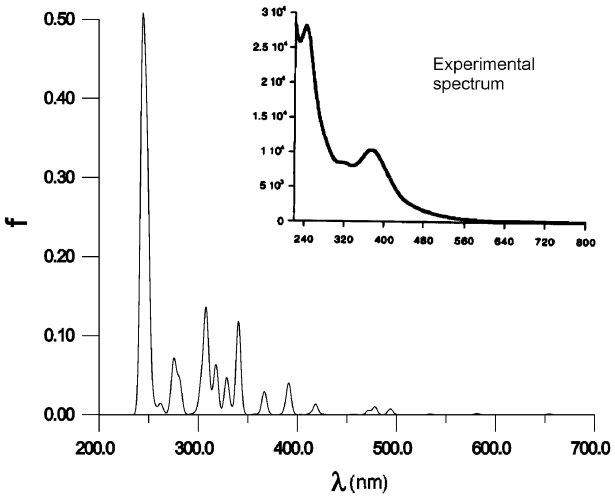

Fig. 3 Electronic spectrum of RRS calculated with the UB3LYP method (PCM solvent model, water as solvent). The experimental spectrum from ref. 35 is also shown.

Table 3 Calculated transition energies, wavelengths, oscillator strengths and the most important configurations obtained with the UB3LYP (water) method for RRS

			Configurations			
E/eV	λ/nm	f	HOMO	LUMO	HOMO	LUMO
1.81	683.7	0.0001	53α(S-NO)	→ 54α(NO-d)	53β(S-NO)	→ 54β(NO-d)
			53α(S-NO)	→ 55α(d-NO)	53β(S-NO)	→ 55β(d-NO)
1.89	654.1	0.0010	53α(S-NO)	→ 54α(NO-d)	53β(S-NO)	→ 54β(NO-d)
			53α(S-NO)	→ 55α(d-NO)	53β(S-NO)	→ 55β(d-NO)
			53α(S-NO)	→ 57α(d-NO)	53β(S-NO)	→ 57β(d-NO)
2.13	581.4	0.0016	45α(NO-d)	→ 59α(d-NO)	45β(NO-d)	→ 59β(d-NO)
			51α(NO-S)	→ 56α(NO)	51β(NO-S)	→ 56β(NO)
			52α(S)	→ 58α(NO)	52β(S)	→ 58β(NO)
			52α(S)	→ 59α(d-NO)	52β(S)	→ 59β(d-NO)
2.32	534.1	0.0010	52α(S)	→ 56α(NO)	52β(S)	→ 56β(NO)
2.50	494.8	0.0043	53α(S-NO)	→ 54α(NO-d)	53β(S-NO)	→ 54β(NO-d)
			53α(S-NO)	→ 57α(d-NO)	53β(S-NO)	→ 57β(d-NO)
2.59	478.2	0.0100	51α(NO-S)	→ 54α(NO-d)	51β(NO-S)	→ 54β(NO-d)
2.96	418.4	0.0128	50α(d-S)	→ 54α(NO-d)	50β(d-S)	→ 54β(NO-d)
			52α(S)	→ 59α(d-NO)	52β(S)	→ 59β(d-NO)
3.16	391.4	0.0382	50α(d-S)	→ 55α(d-NO)	50β(d-S)	→ 55β(d-NO)
			53α(S-NO)	→ 61α(NO)	53β(S-NO)	→ 61β(NO)
3.38	366.2	0.0145	50α(d-S)	→ 56α(NO)	50β(d-S)	→ 56β(NO)
			52α(S)	→ 62α(d-NO)	52β(S)	→ 62β(d-NO)
3.64	340.6	0.1179	47α(NO)	→ 57α(d-NO)	47β(NO)	→ 57β(d-NO)
3.77	328.6	0.0457	47α(NO)	→ 57α(d-NO)	47β(NO)	→ 57β(d-NO)
			53α(S-NO)	→ 61α(NO)	53β(S-NO)	→ 61β(NO)
3.89	318.0	0.0520	48α(NO-S)	→ 56α(NO)	48β(NO-S)	→ 56β(NO)
4.01	308.4	0.0279	48α(NO-S)	→ 55α(d-NO)	48β(NO-S)	→ 55β(d-NO)
4.02	307.8	0.1005	46α(d-S)	→ 56α(NO)	46β(d-S)	→ 56β(NO)
4.08	303.3	0.0378	47α(NO)	→ 62α(d-NO)	47β(NO)	→ 62β(d-NO)
4.41	281.0	0.0400	46α(d-S)	→ 57α(d-NO)	46β(d-S)	→ 57β(d-NO)
			48α(NO-S)	→ 57α(d-NO)	48β(NO-S)	→ 57β(d-NO)
4.47	276.9	0.0132	44α(d-S)	→ 56α(NO)	44β(d-S)	→ 56β(NO)
4.50	275.3	0.0528	48α(NO-S)	→ 60α(NO)	48β(NO-S)	→ 60β(NO)
			49α(NO-d)	→ 61α(NO)	49β(NO-d)	→ 61β(NO)
4.72	262.3	0.0122	43α(d-NO)	→ 54α(NO-d)	43β(d-NO)	→ 54β(NO-d)
4.98	248.4	0.2984	46α(d-S)	→ 56α(NO)	46β(d-S)	→ 56β(NO)
			46α(d-S)	→ 60α(NO)	46β(d-S)	→ 60β(NO)
5.07	244.1	0.3654	42α(d)	→ 58α(NO)	42β(d)	→ 58β(NO)
			49α(NO-d)	→ 61α(NO)	49β(NO-d)	→ 61β(NO)
5.10	242.9	0.0853	44α(d-S)	→ 60α(NO)	44β(d-S)	→ 60β(NO)
			52α(S)	→ 64α(4p)	52β(S)	→ 64β(4p)

3.2.1 Geometry and electronic structure. The geometry of the two conformers of $[Fe_2(SCH_3)_2(NO)_4]$, optimized at the RB3LYP and UB3LYP levels, is characterized in Table 1, together with the experimental structure.[12,14,23] Similarly as for RRS, the UB3LYP optimized bond lengths are much too long, so the RB3LYP optimized geometry was used in the calculations. The RB3LYP optimized Fe–Fe bond is about 0.1 Å shorter and the Fe–NO bond is about 0.04 Å shorter than the experimental ones. The remaining geometrical parameters are well-reproduced in this method.

Comparison of the geometrical parameters of RRS and RRE leads to the conclusion that alkylation of the S ligand affects noticeably the Fe–NO bonding: Fe–N distance becomes longer, the N–O bond shorter and the Fe–N–O angle larger. This is accompanied by a shift of the nitrosyl stretching bands from 1665 and 1690 cm^{-1} to 1750–4 and 1776–8 cm^{-1},[43] denoting decreased back-donation of electron density from the $Fe_2(\mu\text{-}S)_2$ core to the NO π* orbitals.

The molecular orbitals of RRE(I) and RRE(II) are similar. There is no meaningful participation of the iron 4p orbitals in the lowest unoccupied orbitals. In Fig. 4 several HOMO and LUMO spin-up UB3LYP orbitals of RRE(I) are depicted. HOMO orbitals with a large participation of the iron d orbitals are localized mainly on the left side of the molecule, while these with a large contribution from the π^*_{NO} orbitals are on the right side. In the LUMOs the iron d orbitals are localized on the right side and the NO orbitals on the left side of the molecule. Orbital H59 is a metal-sulfur bond, which, similarly as in RRS, shows the mediation of sulfur in the antiferromagnetic coupling. Due to the neutral character of RRE the solvent has no significant effect on the calculated spectrum; thus, the calculations of electronic transitions were carried out without the PCM model.

In Table 2 the energies, atomic charges and spin densities for RRE(I) and RRE(II) calculated with the UB3LYP method are collected. The energies of isomers I and II are practically equal, which is in accord with experiment.[42] The charges on the iron atoms have small positive values. Similar to RRS, the NO groups bear negative charges, whereas in contrast to RRS the charges on the sulfur atoms are positive. There are large spin densities of opposite sign on the iron atoms in the UB3LYP geometry and a spin density of ~0.8 on each NO group. The NO spin density has the opposite sign to the spin density of the iron atom to which the NO group is bound. The spin coupling in RRE is similar to that in RRS—the $\{Fe(NO)_2\}^9$ unit has $S = 1/2$ arising from antiferromagnetic coupling of the ferric ion ($S = 5/2$) and two NO^- ions (each with $S = 1$), and two such units are antiferromagnetically coupled through SR^- bridges, yielding a total $S = 0$. The spin densities are lower than in RRS, accounting for the smaller spin polarization.

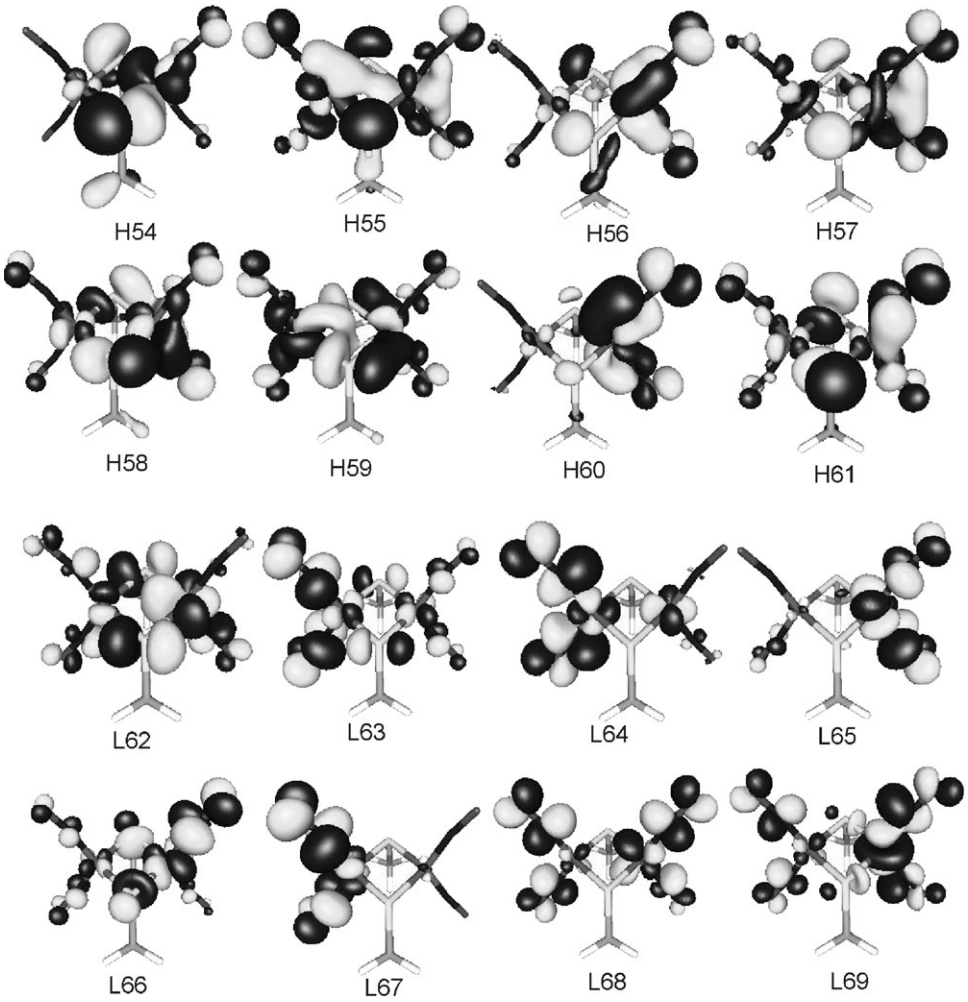

Fig. 4 UB3LYP α (spin-up) HOMO and LUMO orbitals of RRE(I).

3.2.2 Electronic spectrum. The experimental spectrum of Roussin's red esters shows bands at 312 ($\varepsilon = 9 \times 10^3$) and 362 ($8.5 \times 10^3$) nm with a shoulder at 430 nm (4×10^3) and a tail into the green ($\sim 5 \times 10^2$ at 550 nm)[43] or with maxima at 305, 362, 440 and 755 nm;[44] it shows also a steep increase in absorption at $\lambda < 250$ nm. The spectrum is essentially independent of the identity of the R group. Because the low-lying LUMO orbitals do not show large admixtures of the 4p orbitals, the calculations were carried out without any solvent model. The calculated spectra of RRE(I) and RRE(II) are very similar in character and only the spectrum of RRE(I) is described in detail. The calculated spectrum with the UB3LYP method is presented in Fig. 5 with the assumption that isomers I and II are present in equal amounts. As in the case of RRS, there are transitions with large oscillator strengths in the low-energy region of the RB3LYP calculated spectrum. Because of that we present, as for RRS, the results from the UB3LYP calculations only.

The calculated transition energies, wavelengths, oscillator strengths and the most important excitations are presented in Table 4 for the UB3LYP wave function of RRE(I). Only transitions with fairly large oscillator strengths are shown, except for the longest wavelength transitions (over 400 nm), where all calculated transitions are presented. The assigned character of the molecular orbitals involved in the electronic transitions is based on the two atomic orbitals with the largest participation.

The transitions obtained for RRE(I) at 617.0, 611.5 and 582.8 nm with very small oscillator strengths can be generally described as $\pi^*_{NO} \rightarrow$ d LMCT charge transfer transitions and can be attributed to the experimentally very weak band at about 550–755 nm.

The transition calculated at 398.3 nm for RRE(I) can be ascribed to the experimental band at about 430–440 nm. It is composed of $\pi^*_{NO} \rightarrow \pi^*_{NO}$ and d $\rightarrow$ d excitations, with a participation of the sulfur orbitals. The d-d transition is of metel-metal character, mediated by the sulfur orbitals.

The calculated transitions with relatively large oscillator strengths at 350.6 and 345.1 nm for RRE(I) may be compared to the experimental band at 362 nm. These transitions are mixed in character, with d $\rightarrow \pi^*_{NO}$, $\pi^*_{NO} \rightarrow \pi^*_{NO}$ and

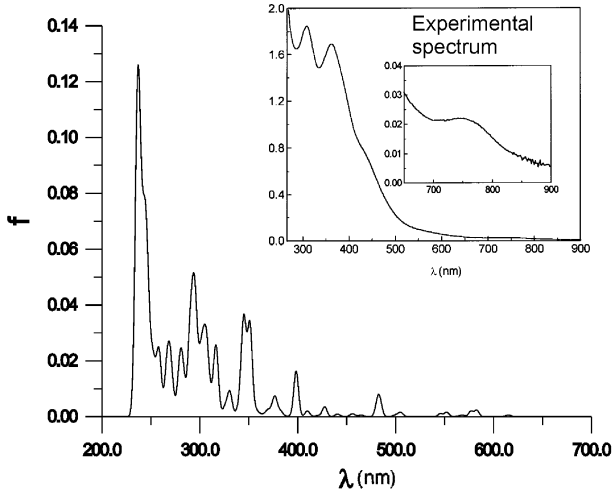

Fig. 5 Electronic spectrum of RRE calculated by the UB3LYP method. The experimental spectrum from ref. 44 is also shown.

Table 4 Calculated transition energies, wavelengths, oscillator strengths and the most important configurations obtained with the UB3LYP method for RRE(I)

			Configurations	
E/eV	λ/nm	f	HOMO LUMO	HOMO LUMO
2.00	617.0	0.0004	60α(NO) → 62α(d-S)	60β(NO) → 62β(d-S)
2.02	611.5	0.0002	60α(NO) → 62α(d-S)	60β(NO) → 62β(d-S)
2.12	582.8	0.0045	58α(NO-d) → 62α(d-S)	58β(NO-d) → 62β(d-S)
			61α(NO-S) → 62α(d-S)	61β(NO-S) → 62β(d-S)
2.56	483.9	0.0092	61α(NO-S) → 67α(NO)	61β(NO-S) → 65β(NO-d)
			58β(NO-d) → 65β(NO-d)	
3.11	398.3	0.0166	59α(d-S) → 62α(d-S)	59β(d-S) → 62β(d-S)
			61α(NO-S) → 63α(NO)	61β(NO-S) → 63β(NO)
3.27	378.2	0.0039	59α(d-S) → 63α(NO)	59β(d-S) → 63β(NO)
3.47	356.6	0.0040	59α(d-S) → 65α(NO-d)	59β(d-S) → 65β(NO-d)
3.53	350.6	0.0303	59α(d-S) → 64α(NO-d)	59β(d-S) → 64β(NO-d)
			61α(NO-S) → 63α(NO)	61β(NO-S) → 63β(NO)
3.59	345.1	0.0405	57α(NO-d) → 69α(d-NO)	57β(NO-d) → 69β(d-NO)
3.91	316.4	0.0190	58α(NO-d) → 63α(NO)	58β(NO-d) → 63β(NO)
			59α(d-S) → 69α(d-NO)	59β(d-S) → 69β(d-NO)
4.06	305.1	0.0284	59α(d-S) → 69α(d-NO)	59β(d-S) → 69β(d-NO)
4.20	294.7	0.0295	54α(S-d) → 62α(d-S)	54β(S-d) → 62β(d-S)
4.21	293.9	0.0479	58α(NO-d) → 66α(d-NO)	58β(NO-d) → 66β(d-NO)
4.65	266.2	0.0240	53α(d-S) → 64α(NO-d)	53β(d-S) → 64β(NO-d)
4.79	258.7	0.0212	55α(d-NO) → 66α(d-NO)	55β(d-NO) → 66β(d-NO)
			57α(NO-d) → 66α(d-NO)	57β(NO-d) → 66β(d-NO)
4.99	248.1	0.0107	56α(d-NO) → 67α(NO)	56β(d-NO) → 67β(NO)
			58α(NO-d) → 67α(NO)	58β(NO-d) → 67β(NO)
5.09	243.3	0.0214	56α(d-NO) → 67α(NO)	56β(d-NO) → 67β(NO)
5.12	242.0	0.0419	56α(d-NO) → 67α(NO)	56β(d-NO) → 67β(NO)
5.20	238.1	0.0569	54α(S-d) → 66α(d-NO)	54β(S-d) → 66β(d-NO)
5.25	235.9	0.1495	52α(d) → 67α(NO)	52β(d) → 67β(NO)
			54α(S-d) → 67α(NO)	54β(S-d) → 67β(NO)
5.29	234.1	0.0175	52α(d) → 67α(NO)	52β(d) → 67β(NO)
			54α(S-d) → 67α(NO)	54β(S-d) → 67β(NO)

π^*_{NO} → d excitations. The transition with larger oscillator strength (at 345 nm, $f = 0.0405$) is of π^*_{NO} → d type.

The transitions with large oscillator strengths at 305.1, 294.7 and 293.9 nm for RRE(I) may be assigned to the experimental band at about 305–312 nm. They can be described as charge transfer transitions having both π^*_{NO} → d and d → π^*_{NO} character with a large participation of the sulfur orbitals. The d → d excitations contribute also to these transitions.

The calculated transitions at 242.0, 238.1 and 235.9 nm for RRE(I) consist mainly of the d → π^*_{NO} excitations. They may be responsible for the steeply increasing absorption at $\lambda < 250$ nm in the experimental spectrum. The transition with the largest oscillator strength occurs in RRE(I) at 235.9 nm ($f = 0.1495$).

The calculated transitions in UB3LYP become symmetrized, similarly as in RRS: the spin-up and spin-down excitations occur with the same (or approximately the same) coefficients; hence the electronic transitions with non-zero oscillator strengths are of the proper symmetry (g or u, in cases where a centre of inversion is present).

3.2.3 Chemical reactivity. The $[Fe_2(SR)_2(NO)_4]$ esters are known to undergo nucleophilic attack on the bridge S atoms, which leads to ring-opening and formation of mononuclear paramagnetic complexes. In the presence of thiolate anions, the reaction results in formation of the monomeric $[Fe(SR)_2(NO)_2]^-$ complexes.

$$[Fe_2(SR)_2(NO)_4] + 2\,RS^- \leftrightarrow 2\,[Fe(SR)_2(NO)_2]^- \qquad (1)$$

Alternatively, ring opening can be followed by a rapid substitution of both RS^- ligands by other nucleophilic anions or solvents, yielding a diversity of monomeric dinitrosylferrates $[FeX_2(NO)_2]^-$ (where X = Br, I, SCN, N_3, NCO, NO_2, DMF, DMSO), with the sporadically detectable mono-substituted $[Fe(SR)X(NO)_2]^-$ intermediate.[12,45]

Nucleophilic attack should engage the LUMO L62 orbital, which is mostly localized on the Fe and S atoms (Fig. 4). Association of a nucleophile is facilitated by the positive charges of both the S atoms in RRE (Table 2). Splitting of the S bridges, which follows the nucleophilic attack and leads to formation of the monomeric $[FeX_2(NO)_2]^-$ complexes [eqn. (1)], is substantiated by the antibonding Fe–S character of the L62 orbital.

$[Fe_2(SR)_2(NO)_4]$ is known for the inactivity of its Fe–NO bond in thermal reactions, and thus its role in promoting the carcinogenic properties of other substances seemed difficult to interpret at one time.[10] However, now it is known that the thiolates present in the human body readily transform the dimer into $[Fe(SR)_2(NO)_2]^-$ monomers, which demonstrate a reactive behaviour of their NO groups. Especially, they are able to produce nitrosothiols:

$$[Fe(SR)_2(NO)_2]^- + R'SH \rightarrow R'S\text{–}NO + \text{decomposition products} \qquad (2)$$

(where SR = L-cysteine or GSH and R′S = albumin).[11,27,46] The two-stage generation of the NO donors, able to promote the carcinogenic action of other species, seems to substantiate the role of RRE in these processes.

A quite different reactivity is demonstrated when RRE solutions are excited by 355 nm radiation.[43] Then RRE undergoes photodissociation of the NO group, followed (in aerated medium) by a complete decomposition. Such behaviour is substantiated by the results of this paper: excitation by radiation within the 362 nm band, assigned to the d → π^*_{NO}, π^*_{NO} → π^*_{NO} and π^*_{NO} → d transitions, should result in weakening and, in consequence, cleavage of the Fe–NO bond.

4. Conclusions

The electronic structure of dimeric nitrosyl-iron complexes emerging from the UB3LYP calculations may be described as composed of two $\{Fe(NO)_2\}^9$ units, in which ferric ion ($S = 5/2$) is antiferromagnetically coupled to two NO^- (each with $S = 1$), giving $S = 1/2$; the units are antiferromagnetically coupled to each other yielding the total $S = 0$. The S^{2-} bridges (in RRS) or SR^- bridges (RRE) mediate the antiferromagnetic coupling.

Generally the calculated spectra are very complicated and many transitions, some of them with very small oscillator strengths, are found. This is in accordance with the experimental spectra, which are rather continuous, with broad bands and tails into the long wavelengths. The calculated transitions are mainly of charge transfer character. On the basis of the UB3LYP calculations the transitions at long wavelengths may be generally described as $\pi^*_{NO} \rightarrow d$ (LMCT), the most intense transitions at the short wavelengths (beyond 250 nm) as $d \rightarrow \pi^*_{NO}$ (MLCT). In the middle part of the spectra both types of transitions are present, but $\pi^*_{NO} \rightarrow d$ transitions still prevail. There are also some $d \rightarrow d$ transitions, but their intensities are relatively weak. A participation of sulfur in the transitions throughout the whole spectrum is evident.

The unrestricted character of the wave functions of RRS and RRE reflects their multiconfigurational nature. The metal-metal bond is very weak or does not exist at all. The nitrosyl-iron bonds are also relatively weak. This is the reason why partially localized molecular orbitals better describe the physical properties of these systems. The attempt to calculate the electronic spectrum on the restricted DFT framework led to transitions with very large oscillator strengths in the long wavelength range, in disagreement with experiment. This arises from the overestimation of the electron density value on the metal-metal axis.

The results of this paper show that the contrasting chemical behaviour of these structurally similar species finds its explanation in their charge distributions and the character of their frontier orbitals. The most outstanding difference in the charge distribution concerns the sulfur atoms, which are negative in RRS and positive in RRE. This distinction is reflected in the opposite susceptibility to undergo electrophilic/nucleophilic attack. In accordance with this, the character of the frontier orbitals favours electrophilic attack in the case of RRS, whereas nucleophilic attack is favoured in the other case. Contrary to the mononuclear $[Fe(SR)_x(NO)_{4-x}]^{n-}$ complexes ($x = 2$ or 3), the dinuclear clusters do not reveal a tendency for homolytic cleavage of the Fe–NO bond in thermal reactions. This behaviour is substantiated by a higher charge on the N atoms in the former case, enabling cleavage *via* a nucleophilic attack.[27] They can, however, behave as NO-donors due to the reactivity of the products of their thermal reactions, which easily split the Fe–NO bonds: that is, RBS in the case of RRS and the $[(RS)_2Fe(NO)_2]^-$ monomer for RRE.

The prevailing character of the $\pi^*_{NO} \rightarrow d$ (LMCT) transitions in both RRS and RRE justifies the similar primary reaction of their excited species, consisting in photodissociation of the NO group.

Acknowledgements

The calculations were performed at the Wrocław Centre for Supercomputing and Networking under computational grant No. 51/96.

References

1 V. Petrouleas, J. J. Brand, K. G. Parrett and J. H. Goldbeck, *Biochemistry*, 1989, **28**, 8980.
2 N. B. Ugulava, B. R. Gibney and J. T. Jarrett, *Biochemistry*, 2001, **40**, 8343.
3 T. A. Rouault and R. D. Klausner, *Rev. TIBS*, 1996, **21**, 174.
4 D. C. Rees and J. B. Howard, *Science*, 2003, **300**, 929.
5 L. Noodleman, C. Y. Peng, D. A. Case and J.-M. Muesca, *Coord. Chem. Rev.*, 1995, **44**, 199.
6 L. Noodleman, T. Lovell, T. Liu, F. Himo and R. Torres, *Curr. Opin. Chem. Biol.*, 2002, **6**, 59.
7 R. A. Torres, T. Lovell, L. Noodleman and D. A. Case, *J. Am. Chem. Soc.*, 2003, **125**, 1923.
8 B. L. Lamotte and J.-M. Muesca, *C. R. Acad. Sci., Ser. IIb: Mec., Phys., Chim., Astron.*, 1997, **324**, 117.
9 L. Noodleman and D. A. Case, in *Advances in Inorganic Chemistry*, ed. R. Cammack, Academic Press, San Diego, CA, 1992, vol. **38**, pp. 423–470.
10 A. R. Butler and I. L. Megson, *Chem. Rev.*, 2002, **102**, 1155.
11 P. G. Wang, M. Xian, X. Tang, X. Wu, Z. Wen, T. Cai and J. J. Janczuk, *Chem. Rev.*, 2002, **102**, 1091.
12 A. R. Butler, C. Glidewell and M. H. Li, in *Advances in Inorganic Chemistry*, ed. A. G. Sykes, Academic Press, New York, 1988, vol. **32**, pp. 335–393.
13 S.-S. Sung, Ch. Glidewell, A. R. Butler and R. Hoffmann, *Inorg. Chem.*, 1985, **24**, 3856.
14 (*a*) S. Sinnecker, F. Neese, L. Noodleman and W. Lubitz, *J. Am. Chem. Soc.*, 2004, **126**, 2613; (*b*) L. D. Slep, A. Mijovilovich, W. Meyer-Klaucke, T. Weyermüller, E. Bill, E. Bothe, F. Neese and K. Wieghardt, *J. Am. Chem. Soc.*, 2003, **125**, 15554; (*c*) P. Ghosh, E. Bill, T. Weyermüller, F. Neese and K. Wieghardt, *J. Am. Chem. Soc.*, 2003, **125**, 1293; (*d*) V. Bachler, G. Olbrich, F. Neese and K. Wieghardt, *Inorg. Chem.*, 2002, **41**, 4179; (*e*) D. Herebian, K. E. Wieghardt and F. Neese, *J. Am. Chem. Soc.*, 2003, **125**, 10997.
15 M. J. Frisch, G. W. Trucks, H. B. Schlegel, G. E. Scuseria, M. A. Robb, J. R. Cheeseman, V. G. Zakrzewski, J. A. Montgomery Jr., R. E. Stratmann, J. C. Burant, S. Dapprich, J. M. Millam, A. D. Daniels, K. N. Kudin, M. C. Strain, O. Farkas, J. Tomasi, V. Barone, M. Cossi, R. Cammi, B. Mennucci, C. Pomelli, C. Adamo, S. Clifford, J. Ochterski, G. A. Petersson, P. Y. Ayala, Q. Cui, K. Morokuma, N. Rega, P. Salvador, J. J. Dannenberg, D. K. Malick, A. D. Rabuck, K. Raghavachari, J. B. Foresman, J. Cioslowski, J. V. Ortiz, A. G. Baboul, B. B. Stefanov, G. Liu, A. Liashenko, P. Piskorz, I. Komaromi, R. Gomperts, R. L. Martin, D. J. Fox, T. Keith, M. A. Al-Laham, C. Y. Peng, A. Nanayakkara, M. Challacombe, P. M. W. Gill, B. Johnson, W. Chen, M. W. Wong, J. L. Andres, C. Gonzalez, M. Head-Gordon, E. S. Replogle and J. A. Pople, *GAUSSIAN03 (Revision A.11.4)*, Gaussian, Inc., Pittsburgh, PA, USA, 2002.
16 (*a*) A. D. Becke, *J. Chem. Phys.*, 1993, **98**, 5648; (*b*) P. J. Stevens, F. J. Devlin, C. F. Chablowski and M. J. Frisch, *J. Phys. Chem.*, 1994, **98**, 11623.
17 M. E. Casida, in *Recent Developments and Applications of Modern Density Functional Theory, Theoretical and Computational Chemistry*, ed. J. M. Seminario, Elsevier, Amsterdam, 1996, vol. **4**, pp. 391–439.
18 P. J. Hay and W. R. Wadt, *J. Chem. Phys.*, 1985, **82**, 299.
19 T. H. Dunning, Jr. and P. J. Hay, in *Methods of Electronic Structure Theory*, ed. H. F. Schaeffer III, Plenum Press, New York, 1977, pp. 1–27.
20 (*a*) S. Miertus, E. Scrocco and J. Tomasi, *Chem. Phys.*, 1981, **55**, 117; (*b*) M. Cossi, V. Barone, R. Cammi and J. Tomasi, *Chem. Phys. Lett.*, 1996, **255**, 327.
21 M. Cossi and V. Barone, *J. Chem. Phys.*, 2001, **115**, 4708.
22 L. Xianti, Z. An, L. Shanhao, H. Knliong and L. Jiaxi, *J. Struct. Chem. (Wuhan)*, 1982, **1**, 79.
23 J. T. Thomas, J. H. Robertson and E. G. Cox, *Acta Crystallogr.*, 1958, **11**, 599.
24 R. S. Gall, C. T.-W. Chu and L. F. Dahl, *J. Am. Chem. Soc.*, 1974, **96**, 4019.
25 C. T.-W. Chu and L. F. Dahl, *Inorg. Chem.*, 1977, **16**, 3245.
26 C. T.-W. Chu, F. Y.-K. Lo and L. F. Dahl, *J. Am. Chem. Soc.*, 1982, **104**, 3409.
27 M. Jaworska and Z. Stasicka, *J. Organomet. Chem.*, 2004, **689**, 1702.
28 J. H. Enemark and R. D. Feltham, *Coord. Chem. Rev.*, 1974, **13**, 339.
29 R. Hoffmann, M. M. L. Chen and D. L. Thorn, *Inorg. Chem.*, 1977, **16**, 503.
30 R. Hoffmann, M. M. L. Chen, M. Elian, M. Rossi and D. M. P. Mingos, *Inorg. Chem.*, 1974, **13**, 2666.

31 C. A. Brown, M. A. Pavlosky, T. E. Westre, Y. Zang, B. Hedman, K. O. Hodgson and E. I. Solomon, *J. Am. Chem. Soc.*, 1995, **117**, 715.
32 T. E. Westre, A. DiCicco, A. Filliponi, C. R. Natoli, B. Hedman, E. I. Solomon and K. O. Hodgson, *J. Am. Chem. Soc.*, 1994, **116**, 6757.
33 C. Hauser, T. Glaser, E. Bill, T. Weyermüller and K. Wieghardt, *J. Am. Chem. Soc.*, 2000, **122**, 4352.
34 M. Li, D. Bonnet, E. Bill, F. Neese, T. Weyermüller and K. Wieghardt, *Inorg. Chem.*, 2002, **41**, 3444.
35 J. L. Bourassa and P. C. Ford, *Coord. Chem. Rev.*, 2000, **200**, 887.
36 J. Bourassa, W. DeGraff, S. Kudo, D. A. Wink, J. B. Mitchell and P. C. Ford, *J. Am. Chem. Soc.*, 1997, **119**, 2853.
37 P. C. Ford, J. Bourassa, K. Miranda, B. Lee, I. Lorkovic, S. Boggs, S. Kudo and L. Laverman, *Coord. Chem. Rev.*, 1998, **171**, 185.
38 M. Lewin, K. Fisher and I. Dance, *Chem. Commun.*, 2000, 947.
39 W. Beck, R. Grenz, F. Gotzfried and E. Vilsmaier, *Chem. Ber.*, 1981, **141**, 3184.
40 C. Glidewell, R. J. Lambert, M. E. Harman and M. B. Hursthouse, *J. Chem. Soc., Dalton Trans.*, 1990, 2685.
41 B. Rauchfuss and T. D. Weatherill, *Inorg. Chem.*, 1982, **21**, 827.
42 A. R. Butler, C. Glidewell and I. L. Johnson, *Polyhedron*, 1987, **6**, 1147.
43 C. L. Conrado, J. L. Bourassa, C. Egler, S. Wecskler and P. C. Ford, *Inorg. Chem.*, 2003, **42**, 2288.
44 S. Costanzo, S. Ménage, R. Parello, R. P. Bonomo and M. Fontecave, *Inorg. Chim. Acta*, 2001, **318**, 1.
45 C. Glidewell and I. L. Johnson, *Polyhedron*, 1988, **7**, 1371.
46 A. R. Butler, C. Glidewell, A. R. Hyde and J. C. Walton, *Polyhedron*, 1985, **4**, 737.